Regulating crystallization to maintain balanced carrier mobility via ternary strategy in blade-coated flexible organic solar cells

Lin Zhang [a,*], Fang Yang [a], Xiangchuan Meng [b], Shuzhi Yang [a], Lili Ke [a], Conghua Zhou [a], Hongping Yan [d], Xiaotian Hu [b], Shaohua Zhang [b,**], Wei Ma [c,***], Yongbo Yuan [a,****]

[a] Hunan Key Laboratory for Super Microstructure and Ultrafast Process, School of Physics and Electronics, Central South University, Changsha, 410083, China
[b] Institute of Polymers and Energy Chemistry, School of Materials Science and Engineering, Nanchang University, 999 Xuefu Avenue, Nanchang, 330031, China
[c] State Key Laboratory for Mechanical Behavior of Materials, Xi'an Jiaotong University, Xi'an, 710049, China
[d] SLAC National Accelerator Laboratory, Menlo Park, CA, 94025, USA

ARTICLE INFO

Keywords:
Organic solar cells
Blade-coating
Ternary
Balance
Large-area

ABSTRACT

Regulating the crystallization of donor and acceptor to maintain balanced carrier mobility is of great importance to fabricate efficient organic solar cells (OSCs). Herein, the balanced crystallinity between donor and acceptor was finely controlled in blade-coated OSCs. By adding high crystalline FOIC into PBDB-T:ITIC system, a balanced carrier mobility was achieved, resulting in the much improved fill factor. The optimized ternary device exhibits an increased current density, due to the enhanced light-harvesting efficiency with complementary absorption and the morphology change. Morphology characterization demonstrated that the ternary film exhibits a highly balanced crystallinity between the donor and acceptor on account of the formation of acceptor alloy. Moreover, the ternary film not only possesses a small domain size, but also exhibits a high domain purity as compared to both binary films. Encouragingly, a highest power conversion efficiency (PCE) of 10.68% was obtained for the blade-coated ternary OSCs. In addition, the blade-coated flexible large-area (105 mm^2) OSC based on PBDB-T:ITIC:FOIC ternary system also exhibits a high PCE of 9.81%, showing great potential in the high-throughput fabrication of OSCs.

1. Introduction

Organic solar cells (OSCs) have emerged as a promising approach for energy harvesting due to their light weight, flexibility, solution-processing ability, and up-scalable processibility [1–3]. Especially for the rapidly development of non-fullerene acceptors, state-of-the-art OSCs have achieved great power conversion efficiency (PCE) of over 18% [4]. However, these breakthrough progresses are mostly obtained on spin-coated small-area devices in the laboratory, which is material consumptive and challenging to scale up to large-area fabrication [5,6]. High-throughput preparation of high-efficiency flexible large-area OSCs is one of the significant challenges for their industrial application [6,7]. Therefore, developing large-area printable film-formation technology is of great importance to practical applications [8–11]. Fortunately, blade-coating [12–17] severing as a large-area film-forming technology can be employed to the high-throughput fabrication of OSCs.

Ternary OSCs is an efficient strategy to improve photovoltaic performance due to the enhanced light-harvesting efficiency with complementary absorption [18–20]. Except for broadening light absorption range, the third component in ternary system also plays an important role in manipulating the morphology of active layer [21–27]. It was reported that the third component of BDT-3T-CNCOO adding into PBDTTPD-HT:$PC_{71}BM$ blends facilitates the formation of bicontinuous interpenetrating network structure for efficient charge transportation [28]. Similarly, high crystalline *p*-DTS($FBTTH_2$)$_2$ small molecules were added into PTB7-Th:$PC_{71}BM$ system to enhance the π-π stacking of donor, so as to improve hole mobility [29]. Thus, adding a high crystalline third component is a practical approach to improve light absorption and enhance the crystallization of active layer.

Generally, high carrier mobility is deemed to be a particularly

* Corresponding author.
** Corresponding author.
*** Corresponding author.
**** Corresponding author.
E-mail addresses: lin.zhang@csu.edu.cn (L. Zhang), shz@ncu.edu.cn (S. Zhang), msewma@xjtu.edu.cn (W. Ma), yuanyb@csu.edu.cn (Y. Yuan).

important characteristic in fabricating high-performance OSCs, and low carrier mobility limits the performance improvement [14,30]. Considerable efforts have been devoted to improve carrier mobility through material design and morphology optimization [14]. Meanwhile, the balance between hole mobility and electron mobility is also important. The unbalanced carrier mobility leads to the single charge accumulation and charge-trapping during charge transportation, which reduces device performance. Some photovoltaic devices have high hole mobility or electron mobility, but photovoltaic performance is not much good. IDIC material possesses a much high electron mobility of 2.9×10^{-4} cm^2 V^{-1} s^{-1}, but PDBT-T1:IDIC based device only exhibits a PCE of 8.71% [31]. Although PTB7-Th:ITIC based device presents a much high hole mobility of 2.8×10^{-3} cm^2 V^{-1} s^{-1}, the optimal device only obtained a unsatisfied PCE of 6.80% with a poor fill factor of 59% [32]. These results should be attributed to the unbalanced carrier mobility, known as buckets effect. Aiming at achieving high-efficiency OSCs, hole mobility and electron mobility not only should be large, but also should keep balanced [14]. Due to the positive correlation between the crystallization and carrier mobility, regulating the crystallization of both donor and acceptor is considered to be an effective method to adjust carrier mobility [14,33]. Therefore, an efficient strategy of controlling crystallization to maintain the balanced crystallinity and carrier mobility between donor and acceptor is of great desire to achieve high photovoltaic performance in blade-coated ternary OSCs.

Herein, a balanced crystallinity of donor and acceptor was finely controlled in blade-coated ternary OSCs by adding high crystalline FOIC into PBDB-T:ITIC system. The ternary system not only displays balanced crystallinity of donor and acceptor, but also possesses pure and small domains. Thus, A highest PCE of 10.68% was achieved for PBDB-T:ITIC:FOIC based ternary device due to the complementary absorption and highly balanced carrier mobility. In addition, the flexible large-area organic solar cell was also fabricated by blade-coating, and shows a great PCE of 9.81%.

2. Results and discussion

The chemical structures of PBDB-T, ITIC and FOIC are shown in Fig. 1a, and a diagrammatic drawing of blade-coating is displayed in Fig. 1b. Fig. 1c presents the energy level diagrams of all materials used in the ternary OSCs. The highest occupied molecular orbital (HOMO) and lowest unoccupied molecular orbital (LUMO) levels are −5.33/-2.92 eV for PBDB-T, −5.51/-3.78 eV for ITIC, and −5.36/-3.92 eV for FOIC, respectively [32,34–37]. The band gap of FOIC is much too small (1.44 eV), corresponding to strong absorption in infrared light. The normalized UV–vis absorption spectra of corresponding neat films are displayed in Fig. 1d. These materials exhibit different absorption bands with strong absorption in the ranges of 500–650 nm, 600–750 nm, 700–900 nm for PBDB-T, ITIC and FOIC, respectively, which forms a complementary absorption in the visible region.

Bulk heterojunction organic solar cells with a conventional device configuration of ITO/PEDOT:PSS/PBDB-T:ITIC:FOIC/ZrAcac (zirconium acetylacetonate)/Al were fabricated by blade-coating in ambient environment. The weight ratio of donor and acceptors were kept at 1:1, while the acceptor composition was varied. The effective device area is 4 mm^2. The current density-voltage (*J-V*) characteristics are shown in Fig. 2a, Fig. S1, and the corresponding photovoltaic parameters are summarized in Table 1, Table S1. For the blade-coated PBDB-T:ITIC device, a PCE of 9.32% with the open-circuit voltage (V_{oc}) of 0.90 V, short-circuit current (J_{sc}) of 15.6 mA cm^{-2}, fill factor (FF) of 66.6%, was obtained. The relatively low J_{sc} limited the further improvement of photovoltaic performance, caused by the limited absorption range and the morphology of active layer. However, PBDB-T:FOIC based device exhibits a much higher J_{sc} (22.5 mA cm^{-2}) due to the broad absorption range. But the V_{oc} (0.72 V) and FF (61.8%) are very low, resulting in a PCE of 9.91%. The small V_{oc} is attributed to the small difference value between the HOMO value of PBDB-T and the LUMO value of FOIC. For the optimized ternary (PBDB-T:ITIC:FOIC) device (FOIC content is 10% in acceptor), the V_{oc} is slightly decreased to 0.89 V as compared to PBDB-T:ITIC based device. But the J_{sc} significantly increased to 17.2 mA cm^{-2} due to the enhanced light-harvesting efficiency with complementary

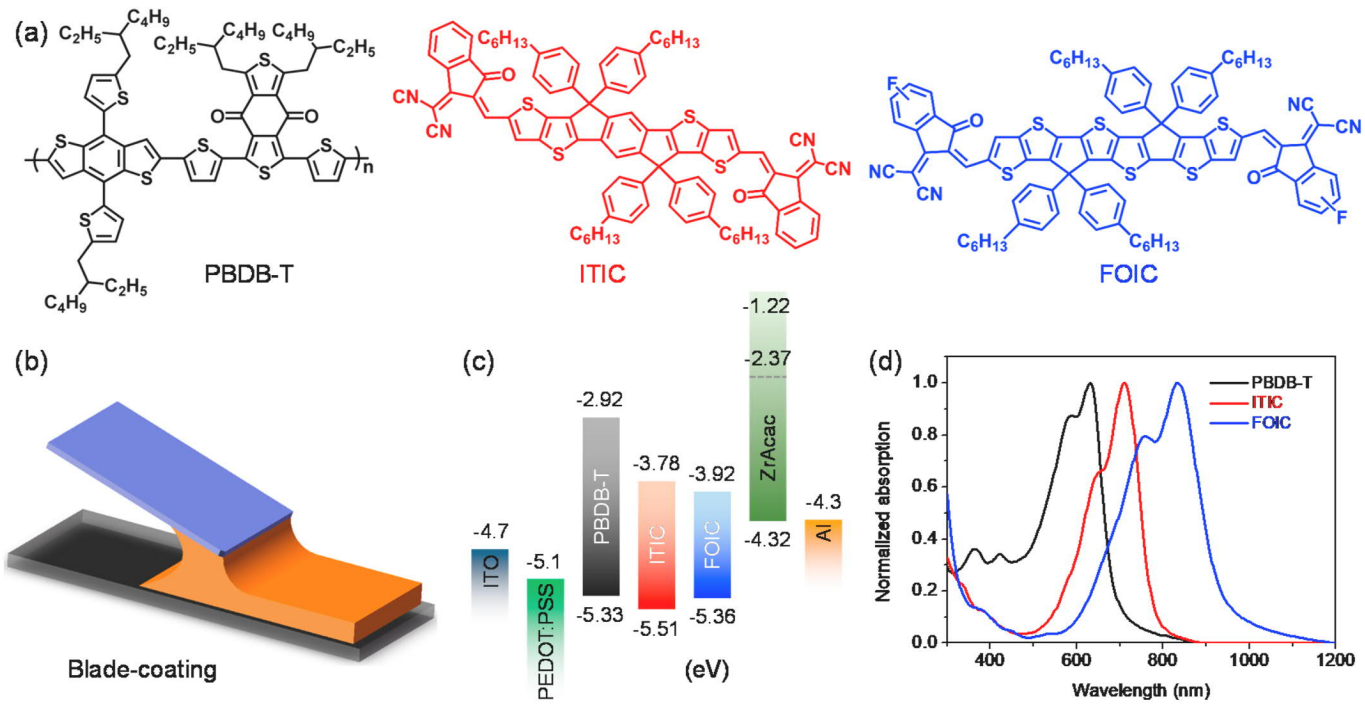

Fig. 1. (a) Chemical structure of PBDB-T, ITIC and FOIC. (b) The diagrammatic drawing of blade-coating. (c) Energy diagrams of all materials used in the ternary solar cells. (d) Normalized UV–vis absorption spectra of neat PBDB-T, ITIC, and FOIC films.

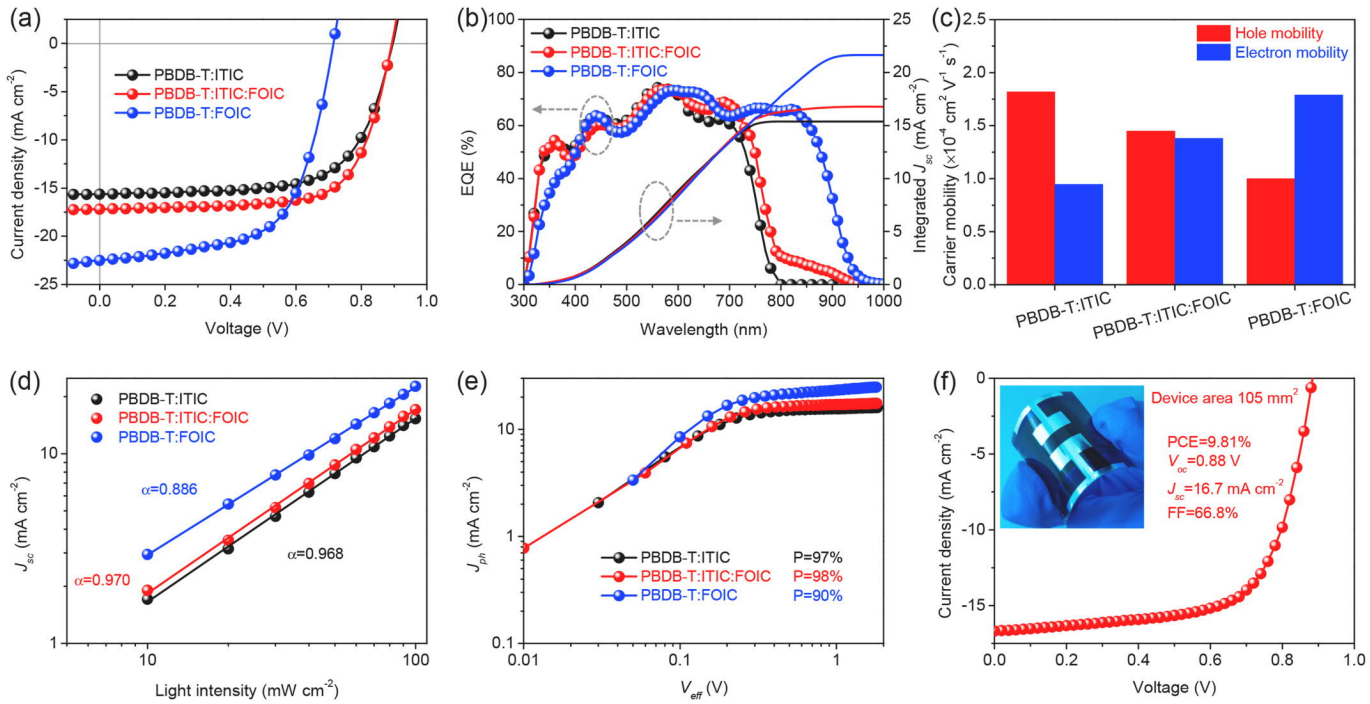

Fig. 2. (a) *J-V* curves, (b) EQE curves and (c) summarized carrier mobility of optimized binary and ternary devices. (d) Short-circuit density versus light intensity plots and (e) photocurrent versus effective voltage of binary and ternary OSCs. (f) *J-V* characteristic of flexible ternary OSC.

Table 1
Photovoltaic parameters of blade-coated binary and ternary OSCs under AM 1.5G 100 mW cm^{-2} illumination.

Active layer	V_{oc} [V]	J_{sc} [mA cm^{-2}]	FF [%]	PCE_{max} (PCE_{ave})[a] [%]	μ_h [cm^2 V^{-1} s^{-1}]	μ_e [cm^2 V^{-1} s^{-1}]
PBDB-T: ITIC	0.90	15.6	66.6	9.32 (9.11)	1.82×10^{-4}	9.46×10^{-5}
PBDB-T: ITIC: FOIC	0.89	17.2	69.8	10.68 (10.39)	1.45×10^{-4}	1.38×10^{-4}
PBDB-T: FOIC	0.72	22.5	61.8	9.91 (9.68)	1.00×10^{-4}	1.79×10^{-4}

[a] Average values are obtained from 15 devices.

absorption and the morphology change of film which will be discussed below. Furthermore, a great FF (69.8%) was obtained for the optimized ternary device, which is much higher than both binary devices, resulting in the highest PCE (10.68%). The J_{sc} variations were confirmed by external quantum efficiency (EQE) measurements [36] (Fig. 2b). PBDB-T:ITIC based binary device exhibits a high EQE response in the wavelength range of 350–750 nm, while PBDB-T:FOIC based binary device displays a strong EQE response in a wide wavelength range of 350–900 nm. Notably, PBDB-T:ITIC:FOIC based ternary device shows an enhanced EQE response in large wavelength as compared to PBDB-T: ITIC based binary device, which should be attributed to the light absorption of FOIC and the morphology variation of film. The integrated J_{sc} of PBDB-T:ITIC, PBDB-T:ITIC:FOIC and PBDB-T:FOIC based devices are 15.4 mA cm^{-2}, 16.8 mA cm^{-2} and 21.7 mA cm^{-2}, respectively, which are consistent with the results from *J-V* measurements. In addition, the flexible large-area device (105 mm^2) based on PBDB-T:ITIC: FOIC system was also fabricated by blade-coating in air, and exhibits a great PCE of 9.81% with the V_{oc} of 0.88 V, J_{sc} of 16.7 mA cm^{-2}, FF of 66.8% (Fig. 2f and Fig. S2).

The charge carrier mobility was determined by space charge limited current (SCLC) [38–40] model. As can be seen in Fig. 2c, Fig. S3 and Table 1, PBDB-T:ITIC based device presents a much higher hole mobility ($\mu_h = 1.81 \times 10^{-4}$ cm^2 V^{-1} s^{-1}) than electron mobility ($\mu_e = 9.46 \times 10^{-5}$ cm^2 V^{-1} s^{-1}). However, for PBDB-T:FOIC based device, the electron mobility (1.79×10^{-4} cm^2 V^{-1} s^{-1}) is pronounced higher than hole mobility (1.00×10^{-4} cm^2 V^{-1} s^{-1}). Both binary devices exhibit unbalanced carrier mobility, resulting in much charge accumulation and recombination. Impressively, a balanced mobility with the hole mobility of 1.45×10^{-4} cm^2 V^{-1} s^{-1} and electron mobility of 1.38×10^{-4} cm^2 V^{-1} s^{-1} was obtained for PBDB-T:ITIC:FOIC based ternary device. Thus, the ternary device possesses a high FF of 69.8% and a great PCE of 10.68%. To get a deep insight of charge recombination dynamics, the light intensity dependent J_{sc} and V_{oc} were performed. As shown in Fig. 2d, the fitted slops (α) are 0.968, 0.970 and 0.886 for PBDB-T:ITIC, PBDB-T:ITIC:FOIC and PBDB-T:FOIC based devices, respectively, while 1 represents that all dissociated free carriers are collected at corresponding electrodes without charge recombination [41,42]. The ternary device exhibits the largest value of α = 0.970, suggesting the weakest bimolecular recombination. As displayed in Fig. S4, the ternary device shows a very small slope of 1.08 *k*T/q, revealing that the trap-assisted recombination or Shockley-Read-Hall was efficiently suppressed [43, 44]. In addition, the exciton dissociation probabilities [45] (*P*, determined by normalizing the photocurrent density, J_{ph} at saturated current density) obtained from the plots of J_{ph} versus effective voltage (V_{eff}) (Fig. 2e) were calculated to be 97%, 98% and 90% for PBDB-T:ITIC, PBDB-T:ITIC:FOIC and PBDB-T:FOIC based devices, respectively. The results indicate that the ternary device has the most effective exciton dissociation efficiency and charge extraction efficiency.

To correlate the improved photovoltaic performance and morphology characteristics, resonant soft X-ray scattering (RSoXS) [46–48] measurements were performed. A photon energy of 284.8 eV (Fig. S5) was selected for the high scattering contrast among PBDB-T, ITIC and FOIC while avoiding the high absorption associated with the carbon 1s core level, which would produce background fluorescence and could lead to radiation damage. As shown in Fig. 3, the calculated domain size of binary films are 33.5 nm and 40.7 nm for PBDB-T:ITIC and PBDB-T:FOIC films, respectively. However, PBDB-T:ITIC:FOIC based ternary film shows the smallest domain size of 30.9 nm, which offers more donor/acceptor interface area, contributing to effective

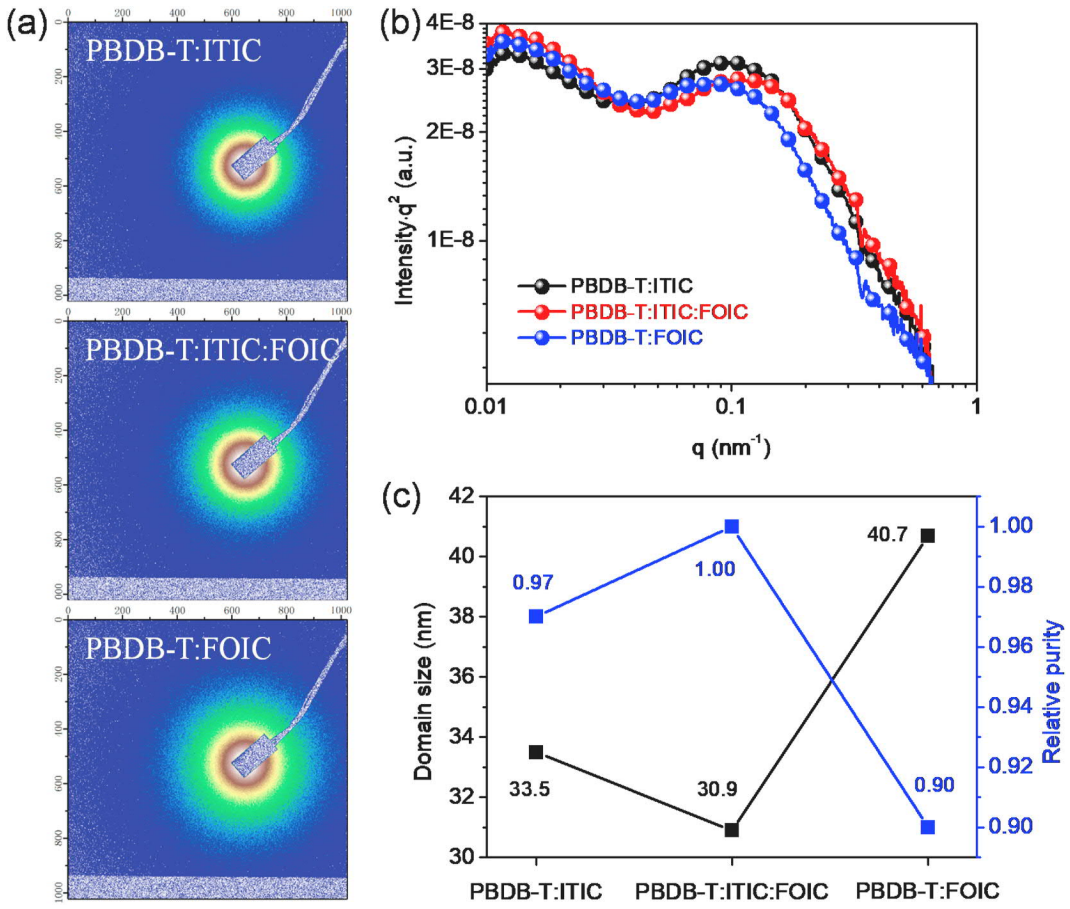

Fig. 3. (a) 2D RSoXS patterns, (b) RSoXS profiles of blade-coated PBDB-T:ITIC, PBDB-T:ITIC:FOIC, PBDB-T:FOIC films and (c) corresponding domain parameters.

exciton dissociation. In addition, ternary film exhibits a higher relative purity (1.00) according to the total scattering intensity analysis than both binary films (0.97 and 0.90), where high purity is beneficial for improving charge transport and decreasing carrier recombination.

To analyze the detailed information of molecular ordering and crystallization behavior, grazing incident wide angle X-ray scattering (GIWAXS) [49] measurements for various films were performed. As displayed in Fig. S6, all these three neat films (PBDB-T, ITIC, FOIC) prefer face-on orientation, as indicated by the much stronger scattering intensity of (010) peak in the out-of-plane direction than the in-plane direction. As shown in Fig. 4, all these three materials maintain the dominant face-on orientation in the blending films. The pronounced diffraction peaks at $q = 0.29$ Å^{-1} and $q = 1.67$ Å^{-1} were considered as the lamellar stacking peak (100) and π-π stacking peak (010) of PBDB-T according to the GIWAXS data of neat PBDB-T film. Similarly, the diffraction peaks at $q = 0.45$ Å^{-1} and $q = 1.80$ Å^{-1} are assigned as the lamellar stacking peak (100) and π-π stacking peak (010) of FOIC. According to the literature [50] and the GIWAXS data of ITIC film, the diffraction peaks at $q \approx 0.35$ Å^{-1}, 0.42 Å^{-1} and 1.48 Å^{-1} originate from the (001) backbone stacking, (100) lamellar stacking and (010) π-π stacking of ITIC. Notably, ITIC exhibits bimodal lamellar stacking in face-on and edge-on directions, as evidenced by the appearance of diffraction peak (100)' at $q \approx 0.46$ Å^{-1}. The calculated d-spacing of edge-on lamellar stacking (13.7 Å) is smaller than that of face-on lamellar stacking (15.0 Å), suggesting that the lamellar stacking of ITIC is tighter in the out-of-plane direction [50]. Notably, PBDB-T:ITIC film displays a higher crystallization of PBDB-T than ITIC, due to the much stronger and sharper diffraction (100), (010) peaks of PBDB-T, leading to the higher hole mobility than electron mobility. However, A higher crystallization of FOIC than PBDB-T was observed for PBDB-T:FOIC film, according to the calculated crystallization coherence length (CCL) [51] values (2.09 nm and 3.35 nm for PBDB-T and FOIC, respectively) (Table 2, Table S2 and Fig. S7). The result was consistent with the difference of hole mobility and electron mobility for the blade-coated PBDB-T:FOIC film. As 10% high crystalline FOIC was incorporated into PBDB-T:ITIC (ternary film), the CCL value of ITIC increased from 3.14 to 3.75 nm, and the CCL value of PBDB-T decreased from 2.94 to 2.32 nm, suggesting the significantly enhanced crystallinity of ITIC and reduced crystallinity of PBDB-T. Furthermore, the (100) scattering peaks of acceptor for PBDB-T:ITIC and PBDB-T:FOIC films in the out of plane direction appeared at $q \approx 0.48$ Å^{-1} and $q \approx 0.44$ Å^{-1}, respectively. However, for the PBDB-T:ITIC:FOIC ternary film, the scattering peak is at $q \approx 0.46$ Å^{-1}, suggesting the formation of alloy model. The alloy model of ITIC and FOIC was also reported in the quaternary organic solar cell [52]. As shown in Fig. S8, the contact angles of PBDB-T, ITIC and FOIC are 105.2°, 97.2° and 96.7°, suggesting the similar surface energy and good miscibility between ITIC and FOIC, which further clarifies the probably formed alloy model. Thus, a more balanced crystallinity of donor and acceptor was obtained for the blade-coated ternary film. It contributes to the balanced hole mobility and electron mobility, so as to improve the photovoltaic performance. The corresponding diagrammatic drawing was illustrated in Fig. 4c to better understand the morphology variation.

To further understand the morphology evolution, in-situ GIWAXS measurements (Fig. 5a) were performed to explore the crystallization kinetics during blade-coating process [53–59]. Time-dependent GIWAXS profiles are shown in Fig. S9, and the fitting results (by Gaussian fitting) of (010) diffraction peaks were displayed in Fig. 5. Due to the violent disturbance caused by the solvent diffraction peak at $q \approx 1.40$ Å^{-1}, (010) diffraction peaks were fitted in batch to obtain

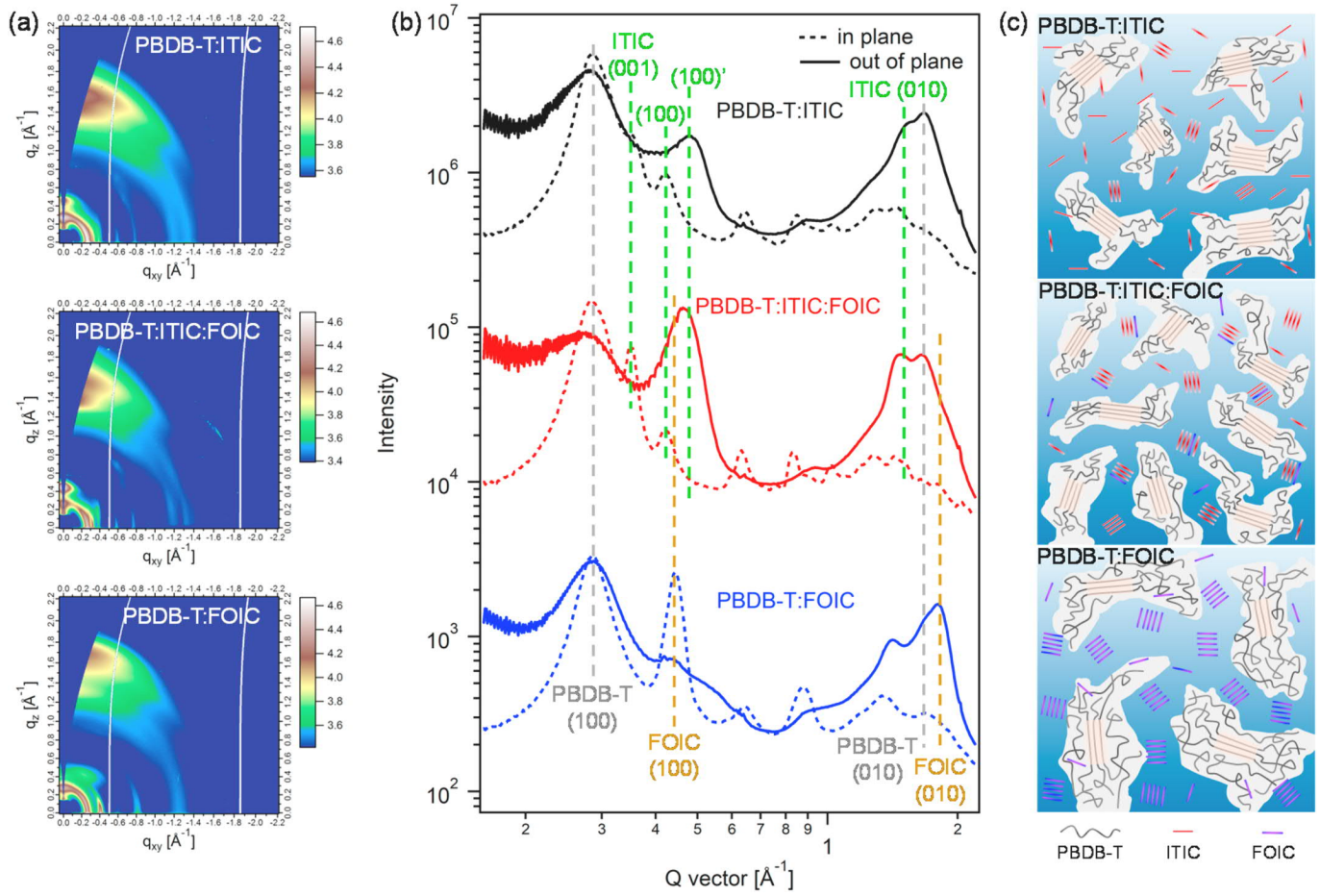

Fig. 4. (a) 2D GIWAXS patterns, (b) line profiles and (c) corresponding diagrammatic drawing of blade-coated PBDB-T:ITIC, PBDB-T:ITIC:FOIC and PBDB-T:FOIC films.

Table 2
Structure parameters obtained by fitting (010) peaks in the out-of-plane from GIWAXS profiles for blade-coated PBDB-T:ITIC, PBDB-T:ITIC:FOIC and PBDB-T:FOIC films.

Active layer	ITIC (010)		PBDB-T (010)		FOIC (010)	
	d_1 (Å)	CCL_1 (nm)	d_2 (Å)	CCL_2 (nm)	d_3 (Å)	CCL_3 (nm)
PBDB-T:ITIC	4.2	3.14	3.7	2.94	/	/
PBDB-T:ITIC:FOIC	4.3	3.75	3.8	2.32	/	/
PBDB-T:FOIC	/	/	3.7	2.09	3.5	3.35

compositive crystallization. The film-formation process can be separated into three stages according to the literature [60]: I) dissolved stage, II) nucleation and growth stage, III) the final dried film stage. Due to the existence of large amount solvents in stage I, no remarkable diffraction information was observed in stage I for all three specimens. However, the beginning time of stage II was different. According to the variation of location and full width at half maximum (FWHM) [51], PBDB-T:ITIC specimen began to nucleate at the time of ≈12.2 s. The nucleation and growth process finished at ≈17.0 s, indicating a slow crystallization process (4.8 s) with the final location of 1.65 $Å^{-1}$ and FWHM value of 0.49 $Å^{-1}$. However, a fast nucleation and growth process was observed for the PBDB-T:FOIC specimen, due to the short stage II (1.2 s), resulting in a final location of 1.78 $Å^{-1}$ and an FWHM value of 0.23 $Å^{-1}$. As compared to PBDB-T:ITIC specimen, the nucleation of ternary specimen occurred much earlier. Moreover, the crystallization process maintained 4.2 s, which is almost the same as the PBDB-T:ITIC specimen, showing the enough time for the crystal growth process. Consequently, it leads to the final location of 1.69 $Å^{-1}$ and the FWHM value of 0.41 $Å^{-1}$. The smaller FWHM value of ternary specimen than PBDB-T:ITIC specimen indicates a higher crystallinity, so as to improve the photovoltaic performance.

3. Conclusions

In conclusion, we fabricated binary and ternary organic solar cells based on PBDB-T:ITIC:FOIC blends by blade-coating in ambient environment, and a high PCE of 10.68% was achieved for the blade-coated ternary organic solar cell. The addition of FOIC into PBDB-T:FOIC blends increases the current density from 15.6 mA cm^{-2} to 17.2 mA cm^{-2}, which is attributed to the enhanced light-harvesting efficiency with complementary absorption and the morphology change. Besides, a high fill factor of 69.8% was obtained due to the much balanced hole mobility and electron mobility as well as the low combination with efficient exciton dissociation and charge extraction for the optimal ternary device. Morphology characterization demonstrated that the ternary film exhibits a highly balanced crystallinity between the donor and acceptor due to the formation of acceptor alloy, resulting in the balanced carrier mobility. Moreover, it was found that the ternary film not only possesses a small domain size, but also exhibits a high domain purity as compared to both binary films. Furthermore, a flexible large-area organic solar cell with the device area of 105 mm^2 was also fabricated by blade-coating in air, and a PCE of 9.81% was achieved. It exhibits great potential in the high-throughput fabrication of organic solar

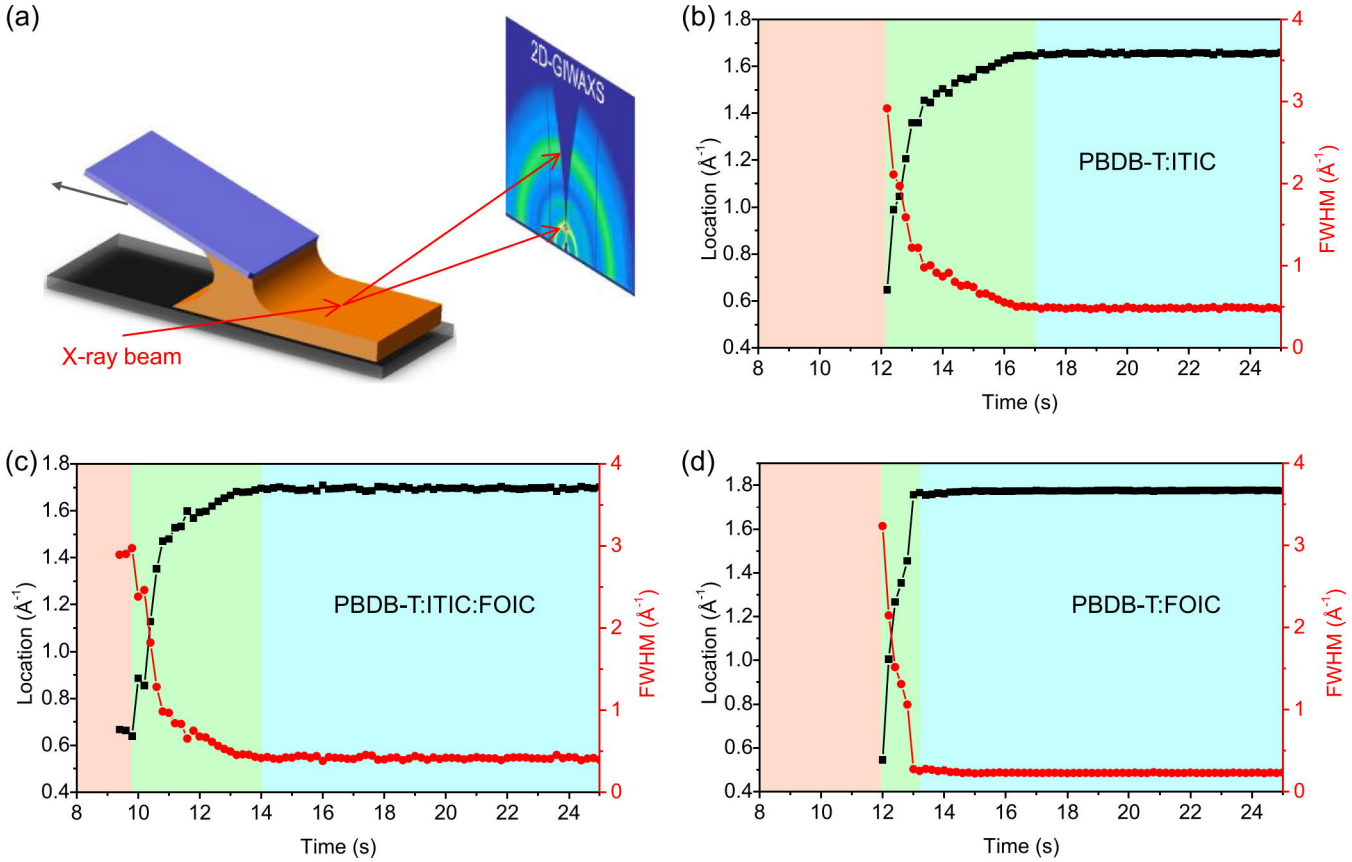

Fig. 5. (a) The diagram of in-situ X-ray scattering for the blade-coating system. Evolution of fitting (010) location, FWHM values for blade-coated (b) PBDB-T:ITIC, (c) PBDB-T:ITIC:FOIC and (d) PBDB-T:FOIC films.

cells and shows excellent prospects in the commercial application.

Declaration of competing interest

The authors declare that they have no known competing financial interests or personal relationships that could have appeared to influence the work reported in this paper.

Acknowledgments

Yongbo Yuan thanks the National Natural Science Foundation of China (51673218) for financial support. Wei Ma thanks for the support from Ministry of Science and Technology of China (No. 2016YFA0200700), NSFC (21704082, 21875182). Shaohua Zhang thanks the Jiangxi Provincial Natural Science Foundation of China (grant no. 20171BAB206012). X-ray data was acquired at beamlines 7.3.3 and 11.0.1.2 at the Advanced Light Source, which is supported by the Director, Office of Science, Office of Basic Energy Sciences, of the U. S. Department of Energy under Contract No. DE-AC02-05CH11231. The authors thank Chenhui Zhu at beamline 7.3.3, and Cheng Wang at beamline 11.0.1.2 for assistance with data acquisition.

Appendix A. Supplementary data

Supplementary data to this article can be found online at https://doi.org/10.1016/j.orgel.2020.106027.

References

[1] R.S. Gurney, D.G. Lidzey, T. Wang, A review of non-fullerene polymer solar cells: from device physics to morphology control, Rep. Prog. Phys. 82 (2019), 036601.
[2] A.S. Gertsen, M.F. Castro, R.R. Sondergaard, J.W. Andreasen, Scalable fabrication of organic solar cells based on non-fullerene acceptors, Flex. Print. Electron. 5 (2020), 014004.
[3] D.L. Li, L. Song, Y.H. Chen, W. Huang, Modeling thin film solar cells: from organic to perovskite, Adv. Sci. 7 (2020) 1901397.
[4] Q.S. Liu, Y.F. Jiang, K. Jin, J.Q. Qin, J.G. Xu, W.T. Li, J. Xiong, J.F. Liu, Z. Xiao, K. Sun, S.F. Yang, X.T. Zhang, L.M. Ding, 18% Efficiency organic solar cells, Sci. Bull. 65 (2020) 272–275.
[5] H.W. Ro, J.M. Downing, S. Engmann, A.A. Herzing, D.M. DeLongchamp, L. J. Richter, S. Mukherjee, H. Ade, M. Abdelsamie, L.K. Jagadamma, A. Amassian, Y. H. Liu, H. Yan, Morphology changes upon scaling a high-efficiency, solution-processed solar cell, Energy Environ. Sci. 9 (2016) 2835–2846.
[6] X.C. Meng, L. Zhang, Y.P. Xie, X.T. Hu, Z. Xing, Z.Q. Huang, C. Liu, L.C. Tan, W. H. Zhou, Y.M. Sun, W. Ma, Y.W. Chen, A general approach for lab-to-manufacturing translation on flexible organic solar cells, Adv. Mater. 31 (2019) 1903649.
[7] W.C. Huang, Z. Jiang, K. Fukuda, X.C. Jiao, C.R. McNeill, T. Yokota, T. Someya, Efficient and mechanically robust ultraflexible organic solar cells based on mixed acceptors, Joule 4 (2020) 128–141.
[8] C.J. Zhang, Q. Luo, H. Wu, H.Y. Li, J.Q. Lai, G.Q. Ji, L.P. Yan, X.F. Wang, D. Zhang, J. Lin, L.W. Chen, J.L. Yang, C.Q. Ma, Roll-to-roll micro-gravure printed large-area zinc oxide thin film as the electron transport layer for solution-processed polymer solar cells, Org. Electron. 45 (2017) 190–197.
[9] Q. Hu, H. Wu, J. Sun, D.H. Yan, Y.L. Gao, J.L. Yang, Large-area perovskite nanowire arrays fabricated by large-scale roll-to-roll micro-gravure printing and doctor blading, Nanoscale 8 (2016) 5350–5357.
[10] X.W. Xu, M. Luo, P. He, J.L. Yang, Washable and flexible screen printed graphene electrode on textiles for wearable healthcare monitoring, J. Phys. D Appl. Phys. 53 (2020) 125402.
[11] X.W. Xu, G.H. Han, H.R. Yu, X. Jin, J.L. Yang, J. Lin, C.Q. Ma, Resistance change of stretchable composites based on inkjet-printed silver nanowires, J. Phys. D Appl. Phys. 53 (2020), 05LT02.
[12] X.D. Gu, L. Shaw, K. Gu, M.F. Toney, Z.N. Bao, The meniscus-guided deposition of semiconducting polymers, Nat. Commun. 9 (2018) 534.

[13] L. Zhang, B.J. Lin, B. Hu, X.B. Xu, W. Ma, Blade-cast nonfullerene organic solar cells in air with excellent morphology, efficiency, and stability, Adv. Mater. 30 (2018) 1800343.

[14] L. Zhang, X.B. Xu, B.J. Lin, H. Zhao, T.F. Li, J.M. Xin, Z.Z. Bi, G.X. Qiu, S.W. Guo, K. Zhou, X.W. Zhan, W. Ma, Achieving balanced crystallinity of donor and acceptor by combining blade-coating and ternary strategies in organic solar cells, Adv. Mater. 30 (2018) 1805041.

[15] L. Zhang, H. Zhao, B.J. Lin, J. Yuan, X.B. Xu, J.N. Wu, K. Zhou, X. Guo, M.J. Zhang, W. Ma, A blade-coated highly efficient thick active layer for non-fullerene organic solar cells, J. Mater. Chem. 7 (2019) 22265–22273.

[16] L. Zhang, H. Zhao, J. Yuan, B. Lin, Z. Xing, X. Meng, L. Ke, X. Hu, W. Ma, Y. Yuan, Blade-coated efficient and stable large-area organic solar cells with optimized additive, Org. Electron. 83 (2020) 105771.

[17] X.W. Xu, M. Luo, P. He, X.J. Guo, J.L. Yang, Screen printed graphene electrodes on textile for wearable electrocardiogram monitoring, Appl. Phys. Mater. Sci. Process 125 (2019) 714.

[18] Y.P. Xie, L.J. Huo, B.B. Fan, H.T. Fu, Y.H. Cai, L. Zhang, Z.Y. Li, Y. Wang, W. Ma, Y. W. Chen, Y.M. Sun, High-performance semitransparent ternary organic solar cells, Adv. Funct. Mater. 28 (2018) 1800627.

[19] Y.P. Xie, F. Yang, Y.X. Li, M.A. Uddin, P.Q. Bi, B.B. Fan, Y.H. Cai, X.T. Hao, H. Y. Woo, W.W. Li, F. Liu, Y.M. Sun, Morphology control enables efficient ternary organic solar cells, Adv. Mater. 30 (2018) 1803045.

[20] X.P. Xu, Z.Z. Bi, W. Ma, Z.S. Wang, W.C.H. Choy, W.L. Wu, G.J. Zhang, Y. Li, Q. Peng, Highly efficient ternary-blend polymer solar cells enabled by a nonfullerene acceptor and two polymer donors with a broad composition tolerance, Adv. Mater. 29 (2017) 1704271.

[21] L. Zhang, W. Ma, Morphology optimization in ternary organic solar cells, Chin, J. Polym. Sci. 35 (2017) 184–197.

[22] L. Zhang, W.H. Zhou, J.M. Shi, T. Hu, X.T. Hu, Y. Zhang, Y.W. Chen, Poly(3-butylthiophene) nanowires inducing crystallization of poly(3-hexylthiophene) for enhanced photovoltaic performance, J. Mater. Chem. C 3 (2015) 809–819.

[23] L. Zhang, M.L. Pu, W.H. Zhou, X.T. Hu, Y. Zhang, Y.P. Xie, B.Q. Liu, Y.W. Chen, Poly(3-butylthiophene) inducing crystallization of small molecule donor for enhanced photovoltaic performance, J. Phys. Chem. C 119 (2015) 23310–23318.

[24] L.J. Li, H. Lin, X. Kong, X.Y. Du, X.W. Chen, L. Zhou, S.L. Tao, C.J. Zheng, X. H. Zhang, pi-pi stacking induced high current density and improved efficiency in ternary organic solar cells, Nanoscale 10 (2018) 9971–9980.

[25] H.X. Jiang, X.M. Li, H. Wang, Z.T. Ren, N. Zheng, X.H. Wang, Y.H. Li, W.C. Chen, R. Q. Yang, Significantly enhanced molecular stacking in ternary bulk heterojunctions enabled by an appropriate side group on donor polymer, Adv. Sci. 7 (2020) 1903455.

[26] Y. Guo, C.C. Shu, D.Y. Dong, F. Nori, Vanishing and revival of resonance Raman scattering, Phys. Rev. Lett. 123 (2019) 223202.

[27] C.C. Shu, Y. Guo, K.J. Yuan, D.Y. Dong, A.D. Bandrauk, Attosecond all-optical control and visualization of quantum interference between degenerate magnetic states by circularly polarized pulses, Opt. Lett. 45 (2020) 960–963.

[28] Y.J. Zhang, D. Deng, K. Lu, J.Q. Zhang, B.Z. Xia, Y.F. Zhao, J. Fang, Z.X. Wei, Synergistic effect of polymer and small molecules for high-performance ternary organic solar cells, Adv. Mater. 27 (2015) 1071–1076.

[29] J.Q. Zhang, Y.J. Zhang, J. Fang, K. Lu, Z.Y. Wang, W. Ma, Z.X. Wei, Conjugated polymer-small molecule alloy leads to high efficient ternary organic solar cells, J. Am. Chem. Soc. 137 (2015) 8176–8183.

[30] Y.J. Zhang, P. He, M. Luo, X.W. Xu, G.Z. Dai, J.L. Yang, Highly stretchable polymer/silver nanowires composite sensor for human health monitoring, Nano Res 13 (2020) 919–926.

[31] Y.Z. Lin, Q. He, F.W. Zhao, L.J. Huo, J.Q. Mai, X.H. Lu, C.J. Su, T.F. Li, J.Y. Wang, J.S. Zhu, Y.M. Sun, C.R. Wang, X.W. Zhan, A facile planar fused-ring electron acceptor for as-cast polymer solar cells with 8.71% efficiency, J. Am. Chem. Soc. 138 (2016) 2973–2976.

[32] Y.Z. Lin, J.Y. Wang, Z.G. Zhang, H.T. Bai, Y.F. Li, D.B. Zhu, X.W. Zhan, An electron acceptor challenging fullerenes for efficient polymer solar cells, Adv. Mater. 27 (2015) 1170–1174.

[33] Y.P. Xie, Y.H. Cai, L. Zhu, R.X. Xia, L.L. Ye, X. Feng, H.L. Yip, F. Liu, G.H. Lu, S.T. Tan, Y.M. Sun, Fibril network strategy enables high-performance semitransparent organic solar cells, Adv. Funct. Mater., DOI: 10.1002/adfm.202002181.

[34] D.P. Qian, L. Ye, M.J. Zhang, Y.R. Liang, L.J. Li, Y. Huang, X. Guo, S.Q. Zhang, Z. A. Tan, J.H. Hou, Design, application, and morphology study of a new photovoltaic polymer with strong aggregation in solution state, Macromolecules 45 (2012) 9611–9617.

[35] W.C. Zhao, D.P. Qian, S.Q. Zhang, S.S. Li, O. Inganas, F. Gao, J.H. Hou, Fullerene-free polymer solar cells with over 11% efficiency and excellent thermal stability, Adv. Mater. 28 (2016) 4734–4739.

[36] T.F. Li, S.X. Dai, Z.F. Ke, L.X. Yang, J.Y. Wang, C.Q. Yan, W. Ma, X.W. Zhan, Fused tris(thienothiophene)-based electron acceptor with strong near-infrared absorption for high-performance as-cast solar cells, Adv. Mater. 30 (2018) 1705969.

[37] S.L. Niu, Z.Y. Liu, N. Wang, Effect of dihydronaphthyl-based C60 bisadduct as third component materials on the photovoltaic performance and charge carrier recombination of binary PBDB-T : ITIC polymer solar cells, Nanoscale 10 (2018) 8483–8495.

[38] J.A. Bartelt, D. Lam, T.M. Burke, S.M. Sweetnam, M.D. McGehee, Charge-carrier mobility requirements for bulk heterojunction solar cells with high fill factor and external quantum efficiency > 90%, Adv. Energy Mater. 5 (2015) 1500577.

[39] B.B. Qiu, J. Yuan, Y.P. Zou, D.J. He, H.J. Peng, Y.F. Li, Z.G. Zhang, An asymmetric small molecule based on thieno 2,3-f benzofuran for efficient organic solar cells, Org. Electron. 35 (2016) 87–94.

[40] S.S. Chen, Y.H. Liu, L. Zhang, P.C.Y. Chow, Z. Wang, G.Y. Zhang, W. Ma, H. Yan, A wide-bandgap donor polymer for highly efficient non-fullerene organic solar cells with a small voltage loss, J. Am. Chem. Soc. 139 (2017) 6298–6301.

[41] X.H. Liu, X.D. Li, L. Wang, J.F. Fang, C.L. Yang, Synergistic effects of the processing solvent and additive on the production of efficient all-polymer solar cells, Nanoscale 12 (2020) 4945–4952.

[42] L. Zhang, B.J. Lin, Z.F. Ke, J.Y. Chen, W.B. Li, M.J. Zhang, W. Ma, A universal approach to improve electron mobility without significant enlarging phase separation in IDT-based non-fullerene acceptor organic solar cells, Nanomater. Energy 41 (2017) 609–617.

[43] A.K.K. Kyaw, D.H. Wang, V. Gupta, W.L. Leong, L. Ke, G.C. Bazan, A.J. Heeger, Intensity dependence of current-voltage characteristics and recombination in high-efficiency solution-processed small-molecule solar cells, ACS Nano 7 (2013) 4569–4577.

[44] C.Y. Long, N. Wang, K.Q. Huang, H.Y. Li, B. Liu, J.L. Yang, Two-step processed efficient perovskite solar cells via improving perovskite/PTAA interface using solvent engineering in PbI2 precursor*, Chin. Phys. B 29 (2020), 048801.

[45] M. Deng, X. Xu, Y.W. Lee, L.K.E. Ericsson, E. Moons, H.Y. Woo, Y. Li, L. Yu, Q. Peng, Fine regulation of crystallisation tendency to optimize the BHJ nanostructure and performance of polymer solar cells, Nanoscale 12 (2020) 12928.

[46] E. Gann, A.T. Young, B.A. Collins, H. Yan, J. Nasiatka, H.A. Padmore, H. Ade, A. Hexemer, C. Wang, Soft x-ray scattering facility at the Advanced Light Source with real-time data processing and analysis, Rev. Sci. Instrum. 83 (2012), 045110.

[47] Y. Wu, Z.Y. Wang, X.Y. Meng, W. Ma, Morphology analysis of organic solar cells with synchrotron radiation based resonant soft X-ray scattering, Prog. Chem. 29 (2017) 93–101.

[48] B.A. Collins, J.E. Cochran, H. Yan, E. Gann, C. Hub, R. Fink, C. Wang, T. Schuettfort, C.R. McNeill, M.L. Chabinyc, H. Ade, Polarized X-ray scattering reveals non-crystalline orientational ordering in organic films, Nat. Mater. 11 (2012) 536–543.

[49] A. Hexemer, W. Bras, J. Glossinger, E. Schaible, E. Gann, R. Kirian, A. MacDowell, M. Church, B. Rude, H. Padmore, A SAXS/WAXS/GISAXS beamline with multilayer monochromator, J. Phys.: Conf. Ser. 247 (2010), 012007.

[50] J.Q. Mai, Y.Q. Xiao, G.D. Zhou, J.Y. Wang, J.S. Zhu, N. Zhao, X.W. Zhan, X.H. Lu, Hidden structure ordering along backbone of fused-ring electron acceptors enhanced by ternary bulk heterojunction, Adv. Mater. 30 (2018) 1802888.

[51] D.M. Smilgies, Scherrer grain-size analysis adapted to grazing-incidence scattering with area detectors, J. Appl. Crystallogr. 42 (2009) 1030–1034.

[52] Z.Z. Bi, Q.L. Zhu, X.B. Xu, H.B. Naveed, X.Y. Sui, J.M. Xin, L. Zhang, T.F. Li, K. Zhou, X.F. Liu, X.W. Zhan, W. Ma, Efficient quaternary organic solar cells with parallel-alloy morphology, Adv. Funct. Mater. 29 (2019) 1806804.

[53] Y.Y. Wang, X. Wang, B. Lin, Z. Bi, X. Zhou, H.B. Naveed, K. Zhou, H. Yan, Z. Tang, W. Ma, Achieving balanced crystallization kinetics of donor and acceptor by sequential-blade coated double bulk heterojunction organic solar cells, Adv. Energy Mater. 10 (2020) 2000826.

[54] B. Lin, X. Zhou, H. Zhao, J. Yuan, K. Zhou, K. Chen, H. Wu, R. Guo, M.A. Scheel, A. Chumakov, S.V. Roth, Y. Mao, L. Wang, Z. Tang, P. Müller-Buschbaum, W. Ma, Balancing the pre-aggregation and crystallization kinetics enables high efficiency slot-die coated organic solar cells with reduced non-radiative recombination losses, Energy Environ. Sci. 13 (2020) 2467.

[55] J. Wang, S. Luo, Y. Lin, Y. Chen, Y. Deng, Z. Li, K. Meng, G. Chen, T. Huang, S. Xiao, H. Huang, C. Zhou, L. Ding, J. He, J. Huang, Y. Yuan, Templated growth of oriented layered hybrid perovskites on 3D-like perovskites, Nat. Commun. 11 (2020) 582.

[56] S.Q. Luo, J.F. Wang, B. Yang, Y.B. Yuan, Recent advances in controlling the crystallization of two-dimensional perovskites for optoelectronic device, Front. Physiol. 14 (2019) 53401.

[57] C.Y. Xie, C.H. Zhou, B. Yang, L. Shen, L.L. Ke, L.M. Ding, Y.B. Yuan, Silicon phthalocyanine passivation for fullerene-free perovskite solar cells with efficient electron extraction, APEX 12 (2019), 064006.

[58] J.Q. Yan, S.Y. Lin, X.C. Qiu, H. Chen, K.M. Li, Y.B. Yuan, M.Q. Long, B.C. Yang, Y. L. Gao, C.H. Zhou, Accelerated hole-extraction in carbon-electrode based planar perovskite solar cells by moisture-assisted post-annealing, Appl. Phys. Lett. 114 (2019) 103503.

[59] X.D. Mo, X. Li, G.Z. Dai, P. He, J. Sun, H. Huang, J.L. Yang, All-inorganic perovskite CsPbBr3 microstructures growth via chemical vapor deposition for high-performance photodetectors, Nanoscale 11 (2019) 21386–21393.

[60] X.D. Gu, H.P. Yan, T. Kurosawa, B.C. Schroeder, K.L. Gu, Y. Zhou, J.W.F. To, S. D. Oosterhout, V. Savikhin, F. Molina-Lopez, C.J. Tassone, S.C.B. Mannsfeld, C. Wang, M.F. Toney, Z.A. Bao, Comparison of the morphology development of polymer-fullerene and polymer-polymer solar cells during solution-shearing blade coating, Adv. Energy Mater. 6 (2016) 1601225.